Check for updates

High Power Laser Science and Engineering, (2025), Vol. 13, e63, 8 pages.
doi:10.1017/hpl.2025.39

HIGH POWER LASER SCIENCE AND ENGINEERING

RESEARCH ARTICLE

A 550 W high-brightness and low-SWaP fiber-coupled pump enabled by double-junction diode chips

Liping Qiu[1,2,3], Hao Yu[2,3], Huadong Pan[2,3], Shaoyang Tan[2,3], Ye Shao[2,3], Yudan Gou[1,3], and Jun Wang[1,2,3]

[1] *College of Electronics and Information Engineering, Sichuan University, Chengdu, China*

[2] *Suzhou Everbright Photonics Co., Ltd., Suzhou, China*

[3] *Jiangsu Key Laboratory of Semiconductor Laser and Sensing Technology, Suzhou, China*

(Received 23 January 2025; revised 5 March 2025; accepted 17 April 2025)

Abstract

Fiber-coupled laser pumps with low size, weight and power consumption (SWaP) have become more and more compelling for applications in both industrial and defense applications. This study presents an innovative approach employing the spectral beam combining technique and double-junction laser diode chips to create efficient, high-power, high-brightness fiber-coupled packages. We successfully demonstrated a wavelength-stabilized pump module capable of delivering over 560 W of ex-fiber power with an electro-optical conversion efficiency of 55% from a 135 μm diameter, 0.22 numerical aperture fiber. The specific mass and volume metrics achieved are 0.34 kg/kW and 0.23 cm^3/W, respectively. The module exhibits a stabilized spectrum with a 3.6 nm consistent interval of two spectral peaks and a 4.2 nm full width at half maximum across a wide range of operating currents.

Keywords: double junction; fiber-coupled module; high brightness; low SWaP; spectral beam combining

1. Introduction

Yb-doped fiber lasers have gained significant traction in defense applications for various equipment platforms due to their exceptional efficiency, reliability and versatility. Currently, semiconductor fiber-coupled modules serve as the primary pump sources for these lasers, facilitating wavelength conversion and output generation. To enhance the performance of these systems, it is crucial to optimize the power-to-weight ratio and power-to-volume ratio of the pump modules. This necessitates the development of configurations that exhibit lower size, weight and power consumption (SWaP) while achieving higher efficiency and brightness than conventional fiber-coupled packages. Specially, a target weight-to-power ratio of less than 0.5 kg/kW and an electro-optical conversion efficiency (PCE) of at least 55% are desired[1].

Recent advancements in diode laser technology have led to significant improvements in brightness and efficiency. Various research groups have successfully enhanced diode laser chip brightness and refined techniques for effectively coupling multiple single emitters into a single fiber[1–8]. For instance, in 2017, Ebert *et al.*[9] demonstrated a laser module prototype capable of 225 μm/0.22 numerical aperture (NA) fiber coupling at 600 W, achieving a weight-to-power ratio of 0.63 kg/kW. In 2020, Kanskar *et al.*[1] reported a similar module with 600 W output and 62% efficiency, resulting in a mass of 0.44 kg/kW. More recently, Xu *et al.*[8] introduced a low-SWaP diode laser pump module delivering 260 W in a 135 μm fiber with a mass of 0.34 kg/kW. These advancements primarily relied on single-junction laser diode (LD) chips, which inherently limit further improvements in brightness and SWaP due to their power constraints.

In this study, we present a novel approach utilizing double-junction diode chips combined with spectral beam combining (SBC) techniques to achieve significantly lower SWaP configurations while enhancing brightness for LD pumps. Our design incorporates an external cavity featuring a multi-layer dielectric grating (MLDG) that combines beams from two emitters within a single chip, effectively mitigating brightness degradation in the fast-axis direction. We demonstrate the successful development of a wavelength-stabilized LD pump source capable of delivering over 560 W continuous-wave (CW) power with

Correspondence to: Y. Gou and J. Wang, College of Electronics and Information Engineering, Sichuan University, Chengdu 610065, China. Emails: gouyudan@scu.edu.cn (Y. Gou); Mike.Wang@everbrightphotonics.com (J. Wang)

© The Author(s), 2025. Published by Cambridge University Press in association with Chinese Laser Press. This is an Open Access article, distributed under the terms of the Creative Commons Attribution licence (https://creativecommons.org/licenses/by/4.0), which permits unrestricted re-use, distribution and reproduction, provided the original article is properly cited.

https://doi.org/10.1017/hpl.2025.39 Published online by Cambridge University Press

PCE exceeding 55% in a 135 μm/0.22 NA fiber at the of temperature of 25°C. The resulting specific mass and volume are measured at 0.34 kg/kW and 0.23 cm^3/W, respectively. To our knowledge, these metrics represent substantial advancements over the existing state-of-the-art.

2. Experiment setup and preparation

2.1. Double-junction chip fabrication and beam quality study in the fast-axis direction

The output power of semiconductor laser chips is a critical parameter influencing their performance. Multi-junction diode architectures, achieved through multiple epitaxially cascaded connections, have proven effective in significantly enhancing single-chip output power[10–12]. This improvement primarily results from a substantial reduction in joule heating during high-current injection, a major limiting factor in traditional single-junction designs. In our previous research, we successfully utilized tunneling junction technology to stack two epitaxial layers, achieving a breakthrough single-chip output power exceeding 132 W, with a corresponding PCE of 60% at 70 A[13]. This highlights the great potential of multi-junction designs in overcoming power and efficiency limitations in high-power semiconductor lasers. In this study, we fabricated double-junction LD chips with a 4.5 mm cavity and a 195 μm emitting width, specifically targeting coupling light in 135 μm fiber. Using metal-organic chemical vapor deposition (MOCVD) technology, the double-junction epitaxial structure was grown on n-type substrates. The quantum wells (QWs) were designed with highly strained indium gallium arsenide (InGaAs) material. A heavily doped GaAs tunnel junction was grown to connect the two active regions, effectively reducing series resistance. The thickness between the two emitters is 3 μm, and the total active region thickness is 4.5 μm. The near-field (NF) size in the fast-axis direction of the entire active region was minimized while maintaining fundamental mode output in the fast axis, simultaneously reducing the thermal gradient between junctions and ensuring subsequent coupling efficiency and brightness of fiber-coupled pump modules. The front facet of the chip was coated with an anti-reflection film with less than 1% reflectivity, enabling good wavelength locking performance at low feedback from the external cavity and reducing power loss due to wavelength locking. The chips were bonded p-side down on SiC substrates using AuSn solder.

The performance metrics are illustrated in Figure 1(a), where the CW output power of the chip exceeds 55 W, and the PCE is recorded at 60.4% with a current of 30 A when tested at 25°C. The NF profile presented at the bottom of Figure 1(b) reveals a uniform spread with an approximate width of 194.2 μm ($1/e^2$) in the slow axis. The NF beam pattern image and optical microscope photograph of the front facet confirm that the NF width in the slow-axis direction

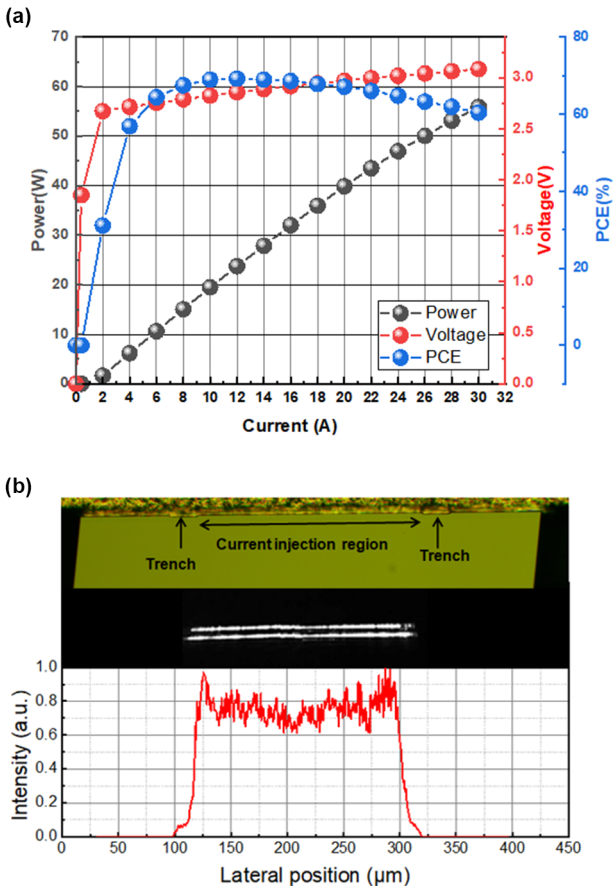


Figure 1. (a) Light-current-voltage (*L-I-V*) results of a 4.5 mm cavity with a 195 μm emitting width double-junction laser diode chip. (b) 100× optical microscope photograph of the front facet, near-field (NF) pattern and intensity profile in the slow-axis direction.

closely matches the current injection width, while the fast-axis direction shows distinct characteristics corresponding to the two active regions as shown in Figure 2(a).

However, due to the larger NF in the fast-axis direction, the beam quality of the double-junction LD chips is reduced compared to that of single emitter chips. The two emitters are positioned off-axis after being collimated by a single fast-axis collimator (FAC) lens, which degrades the brightness of fiber-coupled modules and limits applications requiring optimal brightness levels[14]. To investigate the beam characteristics of double-junction chips post-fast-axis collimation, we designed a setup to measure both the NF and far-field (FF) of the 4.5 mm × 195 μm double-junction LD chip in the fast-axis direction, as depicted in Figure 3.

The experimental setup consists of the following components: a double-junction LD chip mounted on a submount, with a total emitting width of 4.5 μm in the fast-axis direction. The two emitters of the chip are collimated using an FAC lens, F1, which has an effective focal length (EFL) of 600 μm. The FAC lens is positioned at a distance from the LD's front facet equal to its front focal length (FFL). An attenuator in the form of a wedge prism is placed

https://doi.org/10.1017/hpl.2025.39 Published online by Cambridge University Press

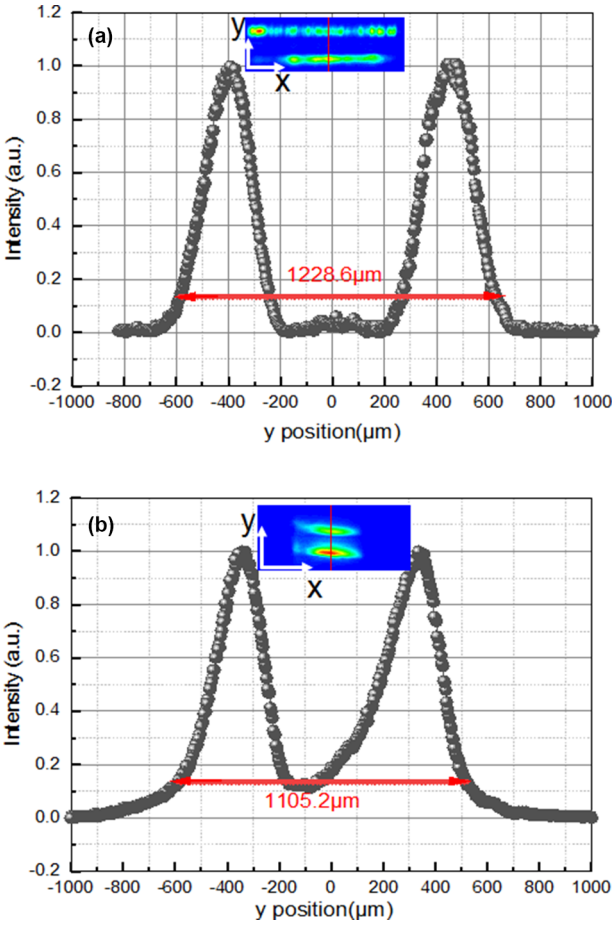


Figure 2. (a) Plot showing the $1/e^2$ intensity of the image profile on the NF CCD, where the calculated full collimated residual angle is 8.19 mrad. (b) Plot showing the $1/e^2$ intensity of the image profile on the FF CCD.

after the collimation to reduce beam intensity and prevent saturation of the charge-coupled device (CCD) detectors while sampling the beam. A 50%:50% beam splitter (BS) divides the collimated beam into two paths.

- NF path: one portion of the beam is focused by a cylindrical lens, F3, with an EFL of 150 mm and imaged onto an NF CCD camera. The NF CCD has a pixel size of 4.8 μm × 4.8 μm.
- FF path: the other portion passes through a cylindrical lens, F2, with an EFL of 200 mm, followed by another cylindrical lens, F3, with an EFL of 150 mm, and is imaged onto an FF CCD camera. The FF CCD has a pixel size of 3.6 mm × 3.6 mm.

Since the total optical path length for beam combination in the LD module (as discussed in Section 2.3) is approximately 120 mm, in the FF test, if the optical path is unfolded, the distance between F1 and F2 is set to the sum of 120 mm and the FFL of F2 to ensure that the collimated beam at 120 mm behind F1 is imaged onto the FF CCD. The magnification in the FF test is determined by the ratio of

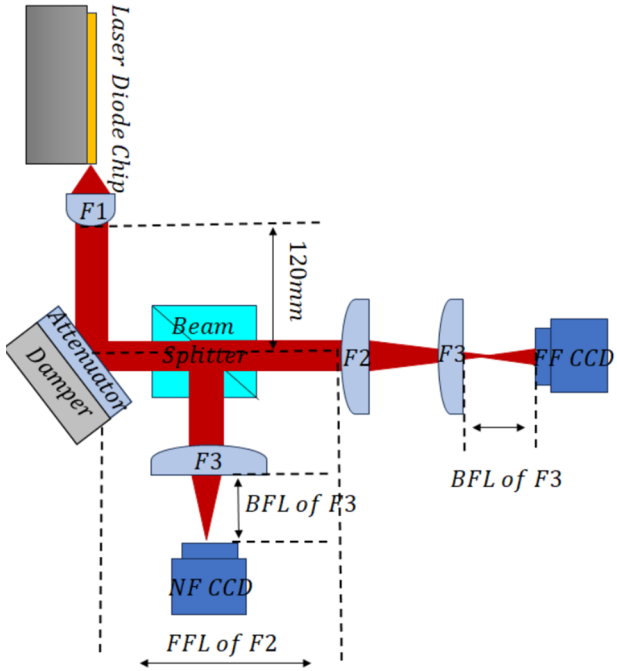


Figure 3. NF and FF test setup diagram of a double-junction laser diode chip. Laser diode chip, double-junction laser diode chip; F1 (FAC), fast-axis collimator of 600 μm EFL; attenuator, uncoated wedge prism; F2 and F3, cylindrical lenses with 200 and 150 mm EFL, respectively, in the fast-axis direction.

the EFLs of F3 to F2, which gives a magnification factor of 0.75×. The test results reveal $1/e^2$ intensity beam width as measured on the NF CCD (1228.6 μm) and FF CCD (1105.2 μm), as shown in Figure 2. The full residual divergence angle of the collimated beam, θ_{FAC}, is calculated to be 1228.6/150 = 8.19 mrad, which aligns closely with the numerical simulation value of 8.3 mrad. Considering the magnification factor of 0.75× in the FF test, the beam width of the collimated beam positioned 120 mm behind FAC lens is determined to be 1473.6 mm. Consequently, the beam-parameter product (BPP) in the fast-axis direction is obtained as follows: (1473.6/2) × (8.19/2) = 3.017 mm · mrad.

The analysis indicates that the beam quality in the fast-axis direction of the double-junction chip significantly deteriorates compared to the typical 0.41 mm · mrad BPP of a single-junction chip. The observed decline in beam quality is primarily due to the larger NF of the double-junction chip. This necessitates further optimization strategies to enhance brightness for applications requiring high-performance fiber-coupled modules.

2.2. Beam quality enhancement of double-junction chips

The SBC technique represents a promising technique for scaling output power and spatial brightness from multiple diode lasers while preserving the beam quality of individual LDs[15,16]. In the study, we employ the SBC technique to

https://doi.org/10.1017/hpl.2025.39 Published online by Cambridge University Press

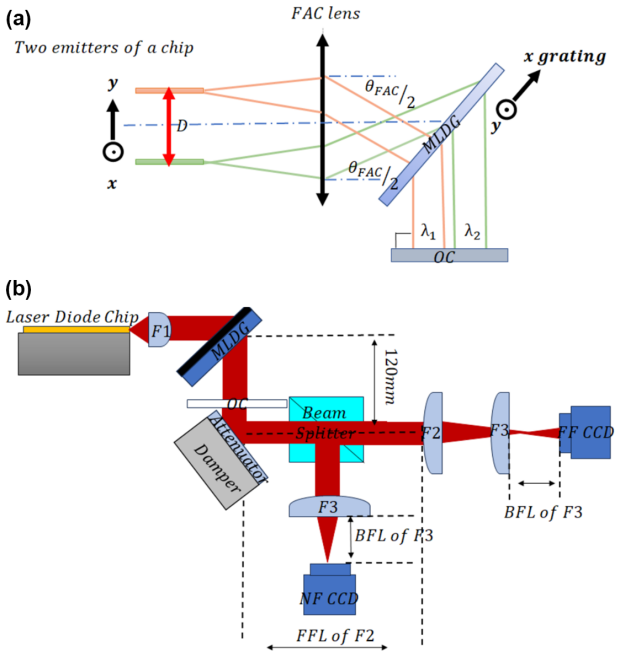


Figure 4. (a) Sketch of the spectral beam-combining external cavity setup consisting of a double-junction chip, an FAC lens, an MLDG and an OC. (b) Schematic diagram showing the NF and FF test setup of the chip after the grating external cavity. F1 (FAC), fast-axis collimator with 600 μm EFL; attenuator, uncoated wedge prism; MLDG, multi-layer dielectric grating; F2 and F3, cylindrical lenses with 200 and 150 mm EFL, respectively, in the fast-axis direction; OC, output coupler.

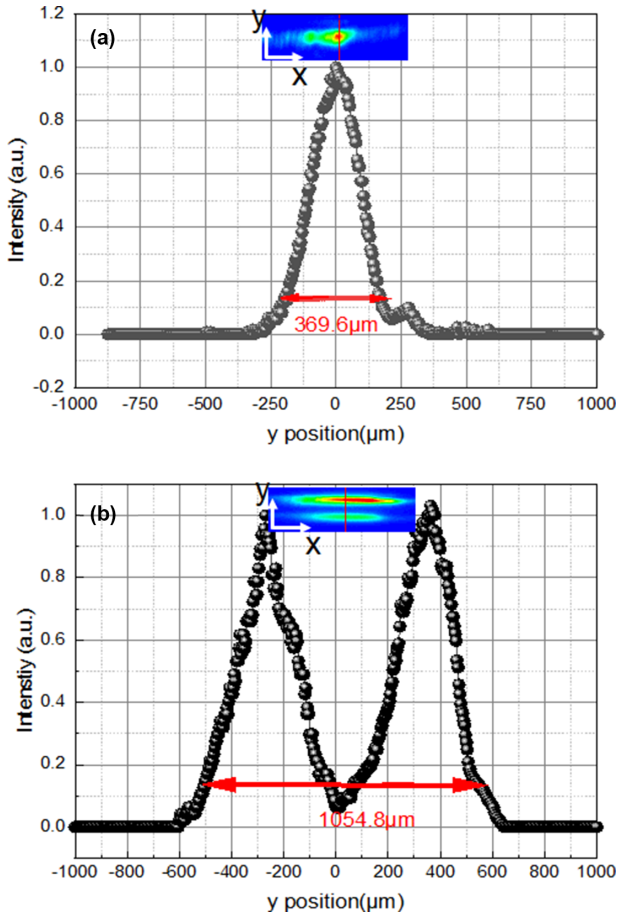


Figure 5. (a) Plot showing the $1/e^2$ intensity of the image profile on the NF CCD, 369.6 μm. The calculated full collimated residual angle after the external cavity is 2.46 mrad. (b) Plot showing the $1/e^2$ intensity of the image profile on the FF CCD, 1054.8 μm.

enhance the beam quality of the double-junction chip in the fast-axis direction. To investigate the improvement in beam quality through SBC, we conducted beam quality tests on the same chip as that in Section 2.1 after passing through a grating external cavity. The experimental setup, schematically shown in Figure 4(b), is similar to that previously described in Figure 3, with the addition of an MLDG and an output coupler (OC). In this configuration, two emitters of the double-junction chip are collimated by a single FAC lens, after which the collimated beams transmit through the MLDG. The grating is oriented with its grooves perpendicular to the fast axis at the Littrow angle. The OC facilitates partial feedback and ensures that both emitters emit at the same diffraction angle. The wavelengths of the two emitters after MLDG λ_1 and λ_2 are determined by their incident angle on the MLDG.

The test result as listed in Figure 5 shows that the $1/e^2$ intensity widths of the image from NF and FF CCD measurements are 369.6 and 1054.8 μm, respectively. The calculated collimated full residual angle θ_{FAC} after passing though the external cavity is 2.46 mrad, based on the expression 369.6/150. Notably, the $1/e^2$ width of the collimated beam remains largely unchanged compared to the measurements taken in Section 2.1. Correspondingly, the BPP in the fast-axis direction is 0.865 mm · mrad, representing an enhancement by a factor of 3.5 times due to the incorporation of the grating in the external cavity. In particular, in SBC here, the combined beam only overlaps in FFs, and that in the NF varies according to the stacking number of chips in the fast-axis direction.

2.3. *High-brightness fiber coupling module configuration*

As schematically shown in Figure 6(a), the design of the high-brightness fiber-coupled module incorporates two rows of seven double-junction chips-on-sub-mount (CoSs). These CoSs are engineered for optimal thermal conductivity and are arranged in a stair–step configuration to facilitate a straightforward mechanical combining architecture. Each diode chip is collimated using a single FAC lens and a slow-axis collimator (SAC) lens. A small 45° turning mirror is positioned after the SAC lens for each collimated beam, allowing the seven beamlets from each row to be vertically stacked. This arrangement directs the beams toward a polarization multiplexer (PBS) that effectively combines the two rows of beams in the slow-axis direction, thereby achieving twice the brightness. Subsequently, the beams pass through a pair of right-angle prisms, which rotate them 90° in the *XY* plane, interchanging the fast-axis and slow-axis

https://doi.org/10.1017/hpl.2025.39 Published online by Cambridge University Press

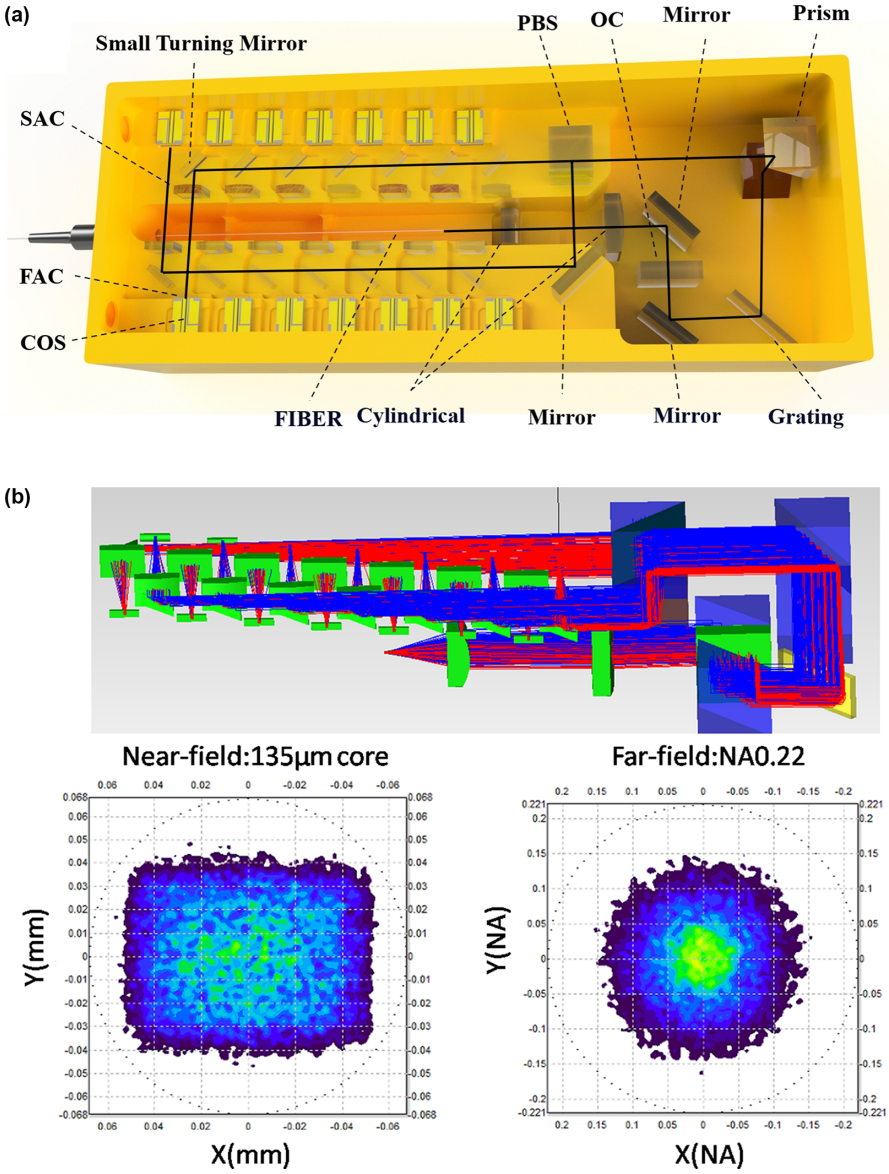


Figure 6. (a) Schematic diagram of the module, taking advantage of the large height of the housing body allowed for integrating cooling channels within its base plate without increasing the volume or mass. (b) Optical model as well as the simulated near field on the fiber input end and far-field ex-fiber.

directions. After the rotation, the beams transmit through an MLDG with a line density of 1500 mm^{-1} and an OC with 5% reflectivity. The MLDG is designed to have –1st-order diffractive angle of 43.3° at 915 nm, with a groove oriented perpendicular to the fast axis. The angle of incidence of the stacked beams on the grating is approximately 45°. The dispersion effects and gain competition lead to the selection of the appropriate wavelength through external optical path feedback. The rotated beams then are focused into a 135 μm diameter fiber using two cylindrical lenses with their optical axes perpendicular to each other. The module employs water cooling through integrated cooling channels within its base plate. To ensure uniform thermal dissipation across all chips, particularly given their varying heights, the cooling channels feature an inclined design. This configuration maintains a consistent distance between each chip and the central axis of the cooling channels, optimizing heat transfer efficiency during CW measurements.

Under 3 L/min water-cooled conditions at 25°C, the spectral characteristics of the module without external cavity feedback were investigated using pulsed parameters of 30 μs pulse width, 1 kHz repetition rate and 3 A driving current. As shown in Figure 7(a), the measured spectrum exhibits a single emission peak at 906.83 nm, corresponding to the 'cold wavelength' of the module under negligible thermal loading.

Subsequently, CW operation was employed to analyze wavelength behavior at varying currents under the same water-cooled conditions. Figure 7(b) demonstrates dual emission peaks under CW conditions, attributed to emissions from the two QWs within the emitter. At higher currents (>8 A), partial spectral overlap between the peaks occurs

https://doi.org/10.1017/hpl.2025.39 Published online by Cambridge University Press

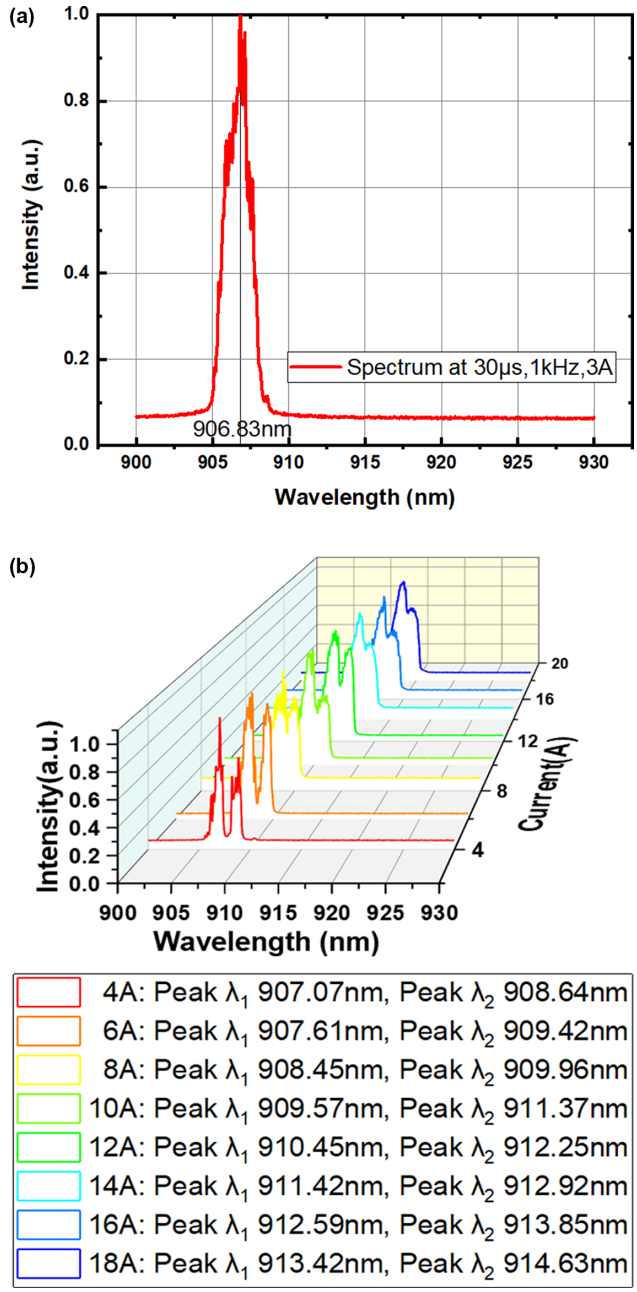


Figure 7. (a) Plot showing the non-stabilized spectrum of the module tested under pulsed current conditions (3 A, 30 μs, 1 kHz). (b) Plot showing the non-stabilized spectrum of the module tested under CW operation and water-cooled conditions (25°C, 3 L/ min flow rate).

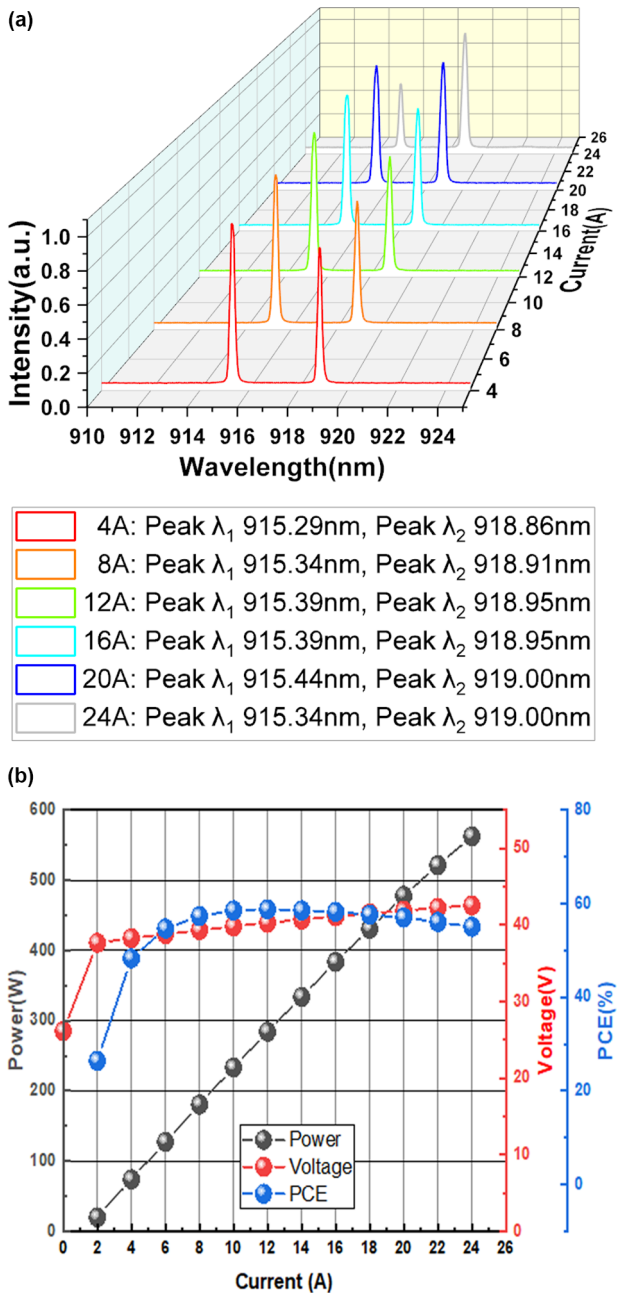


Figure 8. (a) Plot showing the spectrum of the module as a function of the pump current. The interval between the two spectral peaks is approximately constant 3.6 nm. (b) Plot showing *L-I-V* results of the module. The maximal CW output power is 562 W and PCE exceeds 55% at a current of 24 A and a 25°C water flow.

due to thermal-induced gain broadening as the junction temperature rises. The average wavelength separation between the QW peaks across all tested currents is 1.55 nm, corresponding to a 5.1°C temperature difference between the two junctions. This calculation employs a wavelength-temperature coefficient of 0.3 nm/°C. In the 18 A CW test, the junction temperature of the hotter QW is 51.8°C.

The grating equation can be as follows:

$$\sin(\theta) + \sin(\phi) = k\lambda/d. \quad (1)$$

In this equation, θ is the incidence angle, ϕ is the diffractive angle of the grating and k represents the diffraction order, which is set to –1 to maximize diffraction efficiency. All beams experience identical diffraction angles since only those with incidence angles perpendicular to the OC can oscillate and compete for the gain through external cavity optical feedback. The spectral linewidth $\Delta\lambda$ of the grating external cavity is determined by the incidence angle on the grating from the two emitters of the chip, and can be

https://doi.org/10.1017/hpl.2025.39 Published online by Cambridge University Press

described as follows:

$$\Delta\lambda = d \cdot \left[\sin\left(\theta + \frac{\theta_{\mathrm{FAC}}}{2}\right) - \sin\left(\theta - \frac{\theta_{\mathrm{FAC}}}{2}\right) \right]. \quad (2)$$

Here, d denotes the inverse of the line density and θ_{FAC} represents the full residual angle of two collimated emitters from the chip. The value of θ_{FAC} can be derived from the following:

$$\frac{\theta_{\mathrm{FAC}}}{2} = \frac{D}{2f_1}, \quad (3)$$

where D is the total emitting width in the fast-axis direction of the chip, measured at 4.5 μm. By solving Equations (1)–(3) simultaneously, we can determine that the locked wavelength interval $\Delta\lambda$ is approximately 3.61 nm. Figure 8(a) shows the total spectrum of the LD module emission with external cavity as a function of the pump current. Two distinct spectral peaks are observed; the first peak λ_1 and the second peak λ_2 are consistently located at approximately 915.3 and 918.9 nm, respectively. The interval between two spectral peaks remains at around 3.6 nm across a wide range of pump currents, aligning closely with theoretical predictions, which suggest a value of a 3.7 nm. The full width at half maximum (FWHM) of the spectrum is approximately 4.2 nm with 100% power in the bucket from the threshold to full operating power at 24 A. Figure 8(b) demonstrates that the pump module achieves a maximum CW ex-fiber output power of 562 W, with PCE exceeding 55% when operating at a current of 24 A from a 135 μm/0.22 NA fiber. The brightness is 25.5 $\mathrm{MW/(cm^2 \cdot sr)}$. Consequently, this configuration results in specific mass and volume metrics of 0.34 kg/kW and 0.23 $\mathrm{cm^3/W}$, respectively.

3. Conclusion and outlook

In summary, a 4.5 mm cavity with 195 μm emitting width double-junction LD chip is fabricated, achieving a CW output power of 55 W and PCE of 60.4% at a current of 30 A and a temperature of 25°C. Furthermore, by stacking two rows of seven double-junction chips and employing SBC techniques that result in a remarkable improvement in BPP of the double-junction chip by a factor of 3.5 in the fast-axis direction, we designed and demonstrated a low-SWaP wavelength-locked fiber-coupling LD module. This module achieved an impressive ex-fiber output power of 562 W with a PCE exceeding 55% when operating at a case temperature of 25°C. The spectral FWHM was approximately 4.2 nm across a range of pump currents, indicating stable performance. The specific mass and volume metrics of the package were measured at 0.34 kg/kW and 0.23 $\mathrm{cm^3/W}$, respectively, underscoring its suitability for applications requiring compact and efficient laser systems.

In this study, we encountered limitations due to the size constraints of the MLDG, which measures 14 mm × 6 mm. This restriction limited our pump configuration to stacking only seven chips in each row along the fast axis. Theoretically, optimizing the design could allow for 12 chips per row, potentially scaling up the output power of the low-SWaP fiber-coupled module to 960 W in a 135 μm/0.22 NA fiber, representing a record-breaking metric. In addition, the stabilized peak wavelength across a wide range of operating currents is advantageous for applications of Yb-doped fiber lasers, as it allows for effective operation while reducing the cooling system's power requirements. Consequently, this advancement facilitates the miniaturization and weight reduction of laser weapons, making them more portable and efficient. Overall, this research highlights the potential for further advancements in fiber-coupled laser technology, paving the way for enhanced performance in both industrial and defense applications.

To further enhance performance and applicability, another two areas warrant focused investigation. Firstly, under free-running conditions, the temperature gradient ($\Delta T = 5.1$°C) between the two QWs in the double-junction chip induces a wavelength separation of 1.55 nm. Future epitaxial designs could mitigate thermal disparities by adjusting the indium content in the QWs. Such compositional tuning would extend the wavelength locking range. Secondly, the dual-peak separation $\Delta\lambda$ in the locked spectrum is governed by the collimated beam divergence and MLDG groove density. Reducing $\Delta\lambda$ is beneficial for applications with narrow absorption bands. However, this requires trade-offs.

- Increasing the EFL of the FAC lens (f_1) reduces θ_{FAC}, thereby narrowing $\Delta\lambda$. However, this necessitates larger mechanical spacing between chips, complicating alignment and increasing module volume.
- Higher groove densities narrow $\Delta\lambda$ but risk coupling bandwidth limitations if the emitter linewidth exceeds grating acceptance, potentially degrading beam quality[17].
- Minimizing the QW spacing (D) in the fast-axis direction reduces θ_{FAC}, although this may introduce optical coupling losses between active regions.

Addressing these trade-offs will guide future designs toward higher spectral brightness while retaining low-SWaP metrics.

References

1. M. Kanskar, C. Bai, L. Bao, N. Biekert, Z. Chen, M. DeFranza, M. DeVito, K. Fortier, M. Grimshaw, X. Guan, M. Hemenway, S. Li, E. Martin, R. Martinsen, T. Prunty, W. Urbanek, B. Wilkins, J. Zhang, and S. Zhang, Proc. SPIE **10900**, 109000H (2019).

https://doi.org/10.1017/hpl.2025.39 Published online by Cambridge University Press

2. M. Kanskar, L. Bao, Z. Chen, D. Dawson, M. DeVito, W. Dong, M. Grimshaw, X. Guan, M. Hemenway, R. Martinsen, W. Urbanek, and S. Zhang, Proc. SPIE **10514**, 105140L (2018).
3. K. Price, S. Karlsen, P. Leisher, and R. Martinsen, Proc. SPIE **7583**, 758308 (2010).
4. K. Kennedy, M. Hemenway, W. Urbanek, K. Hoener, K. Price, L. Bao, D. Dawson, M. Kanskar, and J. Haden, Proc. SPIE **8965**, 89650D (2014).
5. M. Kanskar, L. Bao, Z. Chen, M. Hemenway, D. Dawson, M. DeVito, W. Dong, M. Grimshaw, X. Guan, K. Kennedy, R. Martinsen, W. Urbanek, and S. Zhang, Proc. SPIE **9348**, 934804 (2015).
6. M. Kanskar, L. Bao, J. Bai, Z. Chen, D. Dahlen, M. DeVito, W. Dong, M. Grimshaw, J. Haden, X. Guan, M. Hemenway, K. Kennedy, R. Martinsen, J. Tibbals, W. Urbanek, and S. Zhang, Proc. SPIE **8965**, 896508 (2014).
7. J. G. Bai, P. Leisher, S. Zhang, S. Elim, M. Grimshaw, C. Bai, L. Bintz, D. Dawson, L. Bao, J. Wang, M. DeVito, R. Martinsen, and J. Haden, Proc. SPIE **7953**, 79531F (2011).
8. D. Xu, Z. Yu, J. Zhang, Y. Wu, Y. Lin, L. Wang, and C. Lang, Proc. SPIE **12867**, 128670Q (2024).
9. C. Ebert, T. Guiney, J. Braker, D. Stapleton, K. Alegria, and D. Irwin, Proc. SPIE **10192**, 101920D (2017).
10. P. Staudinger, W. Pallmann, S. Paul, L. Marigo, S. Marigo, J. Boucart, L. Mutter, and J. Müller, Proc. SPIE **12403**, 1240303 (2023).
11. H. Wenzel, J. Fricke, A. Maaßdorf, N. Ammouri, C. Zink, D. Martin, and A. Knigge, Electron. Lett. **58**, 121 (2022).
12. A. Knigge, A. Klehr, H. Wenzel, A. Zeghuzi, J. Fricke, A. Maaßdorf, A. Liero, and G. Tränkle, Phys. Status Solidi A **215**, 1700439 (2018).
13. J. Wang, S. Tan, Y. Shao, W. Liu, K. Tian, Y. Xiao, Z. Zhang, Y. Gou, L. Zhu, B. Wang, and S. Zhou, Photonics **11**, 258 (2024).
14. R. Todt, R. A. Khadar, S. Riedi, A. Zeghuzi, C. Krammel, M. Rösch, and N. Oliva, Proc. SPIE **12867**, 128670X (2024).
15. H. Meng, X. Ruan, Z. Wang, W. Du, L. Guo, H. Tan, S. Gao, and D. Wu, IEEE Photonics J. **9**, 1501506 (2017).
16. F. Lu, F. Chen, M. Jiang, J. Lee, F. Tian, H. Tan, Y. Ye, W. Zhang, W. Wang, and N. P. Yadav, J. Opt. **52**, 1775 (2023).
17. M. Haas, S. Rauch, S. Nagel, R. Beißwanger, T. Dekorsy, and H. Zimer, IEEE J. Quantum Electron. **53**, 2600111 (2017).

https://doi.org/10.1017/hpl.2025.39 Published online by Cambridge University Press